Applied Catalysis B: Environmental 339 (2023) 123147

Contents lists available at ScienceDirect

Applied Catalysis B: Environmental

journal homepage: www.elsevier.com/locate/apcatb

Dual Cu and S vacancies boost CO_2 photomethanation on $Cu_{1.95}S_{1-x}$: Vacancy-regulated selective photocatalysis

Xian Shi [a,b], Weidong Dai [b], Xing'an Dong [b], Qin Ren [b], Jianping Sheng [b,*], Fan Dong [b]

[a] School of Chemistry and Environmental Engineering, Sichuan University of Science & Engineering, Zigong 643000, China
[b] Research Center for Carbon-Neutral Environmental & Energy Technology, Institute of Fundamental and Frontier Sciences, University of Electronic Science and Technology of China, Chengdu 611731, China

ARTICLE INFO

Keywords:
Copper sulfide photocatalysts
Cu and S dual vacancies
Product selectivity
CO2 photoreduction
Charge transfer

ABSTRACT

Tuning product selectivity and improving activity are significant in CO_2 photoreduction. Herein, we demonstrate that introducing Cu and S dual vacancies on copper sulfide surfaces can improve the CO_2 photoreduction activity and completely switch the selectivity from CO to CH_4. Experimental results reveal that Cu and S vacancies can attain a favorable CH_4 production of 12.42 μmol g^{-1} h^{-1} with 100 % selectivity. Meanwhile, the single S vacancies also exhibit an approx. 4-fold CO yield (13.63 μmol g^{-1} h^{-1}) compared with vacancy-free Cu_2S (3.48 μmol g^{-1} h^{-1}). Mechanism research indicates that the single S vacancies could promote the CO_2 → COOH* → CO* pathway to improve the CO yield, while the simultaneously introducing of Cu and S dual vacancies can further lower the energy barriers of CO_2 → COOH* → HCOOH* → CHO* pathway to promote the stepwise protonation of CO_2, which in turn strengthen the selectivity of CO_2-to-CH_4 photoreduction.

1. Introduction

Solar-driven CO_2 photoreduction offers a sustainable and carbon-neutral tactic to generate value-added chemical products and alleviate energy crises [1]. Constructing efficient photocatalysts is highly desirable as they are the crucial determinant for the activity and selectivity of CO_2 photoreduction [2–4]. Although much progress has been propelled in advanced photocatalyst construction to efficiently improve the reduction activity [5,6], the rebellious product selectivity still limits the practical applications of CO_2 photoreduction [7]. Thus, it is imperative to devise effective methods for modulating product selectivity to enhance the yield of the desired CO_2 photoreduction product.

Maximizing the production of the desired product is crucial in CO_2 photoreduction, as the byproducts generated during the process can compete for photogenerated electrons, occupy active sites, and pose a significant challenge for product separation. Previous reports suggest that constructing well-designed active sites for efficient CO_2 adsorption and activation could be an efficient way to optimize activity and product selectivity. Additionally, efficient separation of charge carriers is also crucial for regulating activity and product selectivity in CO_2 photoreduction reactions, as it impacts the transportation of photogenerated electrons to the active sites [8]. Thus, to achieve efficient and selective CO_2 photoreduction, it is highly desirable to develop a feasible method to create specific active sites and regulate charge carrier dynamics precisely. Unfortunately, no effective and general strategies are available to solve these issues simultaneously, which is imperative for regulating activity and selectivity during CO_2 photoreduction.

Surface vacancies can serve as active sites to enhance the chemisorption of CO_2 and further enable the trapping and transportation of photogenerated electrons to adsorbed CO_2, ultimately improving CO_2 activation and guiding the direction of product evolution. Therefore, manipulating vacancies through surface engineering can help adjust product selectivity by leveraging the unique photoelectrochemical properties of surface vacancies [9–12]. Several recent studies have delved into the multi-step reaction of CO_2 reduction on catalyst surfaces equipped with different vacancies. These investigations, with a focus on copper sulfide photocatalysts as an example, have uncovered the adsorption and activation mechanisms of CO_2 on surface vacancies and highlighted the crucial role of these vacancies in regulating product selectivity [8]. For instance, the Cu vacancies can regulate the electronic structures of $Cu_{1.96}S$, beget the suitable binding energy for intermediates, decrease the charge transfer resistance, and enhance the CO_2 adsorption capacity, thereby achieving high activity and selectivity of CO_2 electroreduction to CO [13]. In addition, it has been

* Corresponding author.
E-mail address: jpshengchn@163.com (J. Sheng).

https://doi.org/10.1016/j.apcatb.2023.123147
Received 25 April 2023; Received in revised form 19 June 2023; Accepted 2 August 2023
Available online 3 August 2023

demonstrated that introducing double S vacancies on the surface of CuS can serve as coupled active sites that boost the production of crucial intermediates, thereby facilitating the selective electrocatalytic reduction of CO_2 to yield C_3 product [14]. Although copper sulfides with a single type of vacancy (either Cu or S vacancy) have been extensively studied for CO_2 electroreduction, they have not been thoroughly investigated for tuning the activity and product selectivity in CO_2 photoreduction. Moreover, other recent studies on BiOCl photocatalysts have indicated that constructing dual oxygen and chlorine vacancies in BiOCl can effectively initiate the activation of O_2, leading to the generation of monatomic reactive oxygen species to boost the photocatalytic elimination of pollutants. This further validates that the influence of dual vacancies on photocatalysis surpasses that of single vacancies [15]. Given the factors mentioned above, we have been naturally inclined to investigate the potential of copper sulfide photocatalysts, specifically those containing dual vacancies of both Cu and S, for CO_2 photoreduction. However, despite the urgency, constructing a copper sulfide catalyst with dual Cu and S vacancies to enhance reduction activity, regulate product selectivity, and unveil the photoreduction mechanism of CO_2 on these vacancies sites remains challenging.

In this work, we report a $Cu_{1.95}S_{1-x}$ photocatalyst with dual Cu and S vacancies (labeled as $Cu_{1.95}S_{1-x}$) as a prototype for selective CO_2-to-CH_4 photoreduction and discuss the activity and product selectivity promotion mechanism. Specifically, compared with the vacancy-free Cu_2S (labeled as Cu_2S), the S vacancies on defective Cu_2S (labeled as Cu_2S_{1-x}) could efficiently enhance the selective CO_2-to-CO photoreduction. Besides, more encouragingly, combining the experimental results with density functional theory (DFT) calculation results, with the introduction of Cu vacancy, the Cu and S dual vacancies could further enhance the adsorption of CO_2 molecules on $Cu_{1.95}S_{1-x}$ and promote the charge carrier transformation, thus boosting the CO_2 photoreduction performances of $Cu_{1.95}S_{1-x}$. Most importantly, the Cu and S dual vacancies could completely switch product selectivity from CO to CH_4. Thus, the photocatalysis proceeded in the direction of producing more valuable CH_4. This work provides a general and effective strategy for tuning the performances of selective CO_2 photoreduction by regulating the surface features of photocatalysts via defect engineering.

2. Experimental

2.1. Sample preparation

$Cu_{1.95}S_{1-x}$: 1 mmol of $CuCl_2{\cdot}2\ H_2O$, 300 mg of CTAB, and 300 mg of $C_6H_{12}N_4$ were dissolved in 40 mL ethylene glycol by continuous stirring, then 1 mmol of CH_3CSNH_2 was added, and the mixtures were continuously stirred for 2 h. Subsequently, the resulting mixtures were heated in a 50 mL of Teflon-lined stainless-steel autoclave at 160 °C for 48 h. The obtained product was washed with ethylene glycol and deionized water many times and finally vacuum-dried at 80 °C for 24 h.

Cu_2S_{1-x}: 1 mmol of $CuCl_2{\cdot}2\ H_2O$ and 300 mg of $C_6H_{12}N_4$ were dissolved in 40 mL ethylene glycol by continuous stirring, then 1 mmol of CH_3CSNH_2 was added, and the mixtures were continuously stirred for 2 h. Subsequently, the resulting mixtures were heated in a 50 mL of Teflon-lined stainless-steel autoclave at 160 °C for 48 h. The obtained product was washed with ethylene glycol and deionized water many times and finally vacuum-dried at 80 °C for 24 h.

Cu_2S: 2 mmol of $Cu(NO_3)_2$ and 1 mmol of CH_3CSNH_2 were dissolved in 40 mL of ethylenediamine by continuous stirring, then the resulting mixtures were heated in a 50 mL of Teflon-lined stainless-steel autoclave at 160 °C for 48 h. The obtained product was washed with ethylene glycol and deionized water many times and finally vacuum-dried at 80 °C for 24 h.

2.2. Characterizations

X-ray diffraction (XRD) were carried out at room temperature (Cu-Kα radiation, D/Max RA, Rigaku Corp., Japan). High-resolution transmission electron microscopy (HRTEM) patterns were obtained using a JEM-2100 F field emission electron microscope (Japan Electronics Co., Ltd, Japan). X-ray photoelectron spectroscopy (XPS) measurements were carried out on a Thermo Scientific ESCALAB 250Xi X-ray photoelectron spectrometer (Al-Kα, 150 W, reference C 1 s = 284.8 eV, Thermo Fisher Scientific, U.S.A). The optical absorption properties were measured by ultraviolet-visible diffuse reflectance spectra (UV–vis DRS) (UV-2450, Shimadzu, Japan). Photoluminescence (PL) spectrum (HITACHI F-7000, Hitachi, Japan) and electrochemical workstation (CST520, Corrtest, China) were used to analyze the photogenerated electron-hole separation efficiency. The photogenerated electrons and S vacancies of samples were confirmed by an electron paramagnetic resonance (ESR) spectrometer (JES-FA200, Japan Electronics Co., Ltd, Japan). DFT calculations were performed by employing the VASP5.4 code, using the generalized gradient approximation with the Perdew-Burke-Ernzerhof exchange-correlation functional, the details were described in supporting information.

2.3. CO_2 photoreduction

The CO_2 photoreduction experiments were carried out in a gas-solid phase reactor in a Labsolar 6 A closed circulation system (Beijing Perfectlight Technology Co., Ltd., China). Firstly, 10 mg of sample was dispersed in 10 mL of distilled water and dried on the surface of a microporous membrane (diameter = 2.0 cm). Subsequently, the reaction system was evacuated, and pure CO_2 was purged through a gas cylinder at a constant pressure of about 1 atm. A 300 W xenon lamp with an AM 1.5 G filter (PLS-SXE300UV, Beijing Perfectlight Technology Co., Ltd., China) was the light source. A circulation cooling system (DC-0506, Shanghai Sunny Hengping Scientific Instrument Co., Ltd., China) was employed to keep the reaction temperature at 298 K. The products were analyzed using a GC2002 gas chromatograph (Shanghai Kechuang Chromatography Instrument Co., Ltd., China).

The yield rate of the product gas [φ(gas)] could be deduced from the equation of state of an ideal gas ($PV = nRT$) and calculated by the following equation when the pressure (P) is 1 atm.

$$Vm'/T1 = Vm/T,$$

$$n' = V'/\ Vm',$$

$$\varphi(\text{gas}) = n'/(t{\cdot}m),$$

where $Vm = 22.4\ \text{L mol}^{-1}$ is the molar volume of gas under standard conditions (P = 101.325 KPa, T = 273.15 K), Vm' is the actual molar volume of gas at reaction pressure (P = 101.325 KPa), $T1$ = 298 K is the reaction temperature, n' is the amount of product gas, V' is the test volume, t is the reaction time, and m is the amount of photocatalyst.

The CO selectivity was evaluated according to the required electrons for CO_2 photoreduction:

$$\text{CO selectivity}\ (\%) = [2\varphi(\text{CO})]/[2\varphi(\text{CO}) + 8\varphi(\text{CH}_4) + 2\varphi(\text{H}_2)] \times 100\ \%{\cdot}$$

2.4. In-situ Fourier transform infrared (FTIR) spectroscopy

Before the adsorption/desorption process, the loaded samples were purged with Ar (50 mL min^{-1}) for 1 h at 150 °C to remove all impurities. The background spectrum was then collected after the chamber temperature was lowered to room temperature. Then the reaction gas mixture (25 mL min^{-1} of Ar and 5 mL min^{-1} of CO_2 with a trace of H_2O vapor) was introduced into the reactor. The variation of the FTIR spectra was recorded to monitor the dynamic adsorption process. After reaching

sorption equilibrium, the background spectrum was collected again. and the FTIR spectra were recorded as a function of time to investigate the CO_2 photoreduction process under light irradiation (a 300 W xenon lamp with an AM1.5 filter).

3. Results and discussion

3.1. Structural features of Cu_2S, Cu_2S_{1-x} and $Cu_{1.95}S_{1-x}$ photocatalysts

The crystal structures of the as-prepared copper sulfide photocatalysts were first investigated by XRD, as shown in Fig. 1a. The XRD pattern of $Cu_{1.95}S_{1-x}$ showed a series of diffraction peaks at 32.19°, 46.12°, and 54.70°, which were ascribed to the (2 0 0), (2 2 0), and (3 1 1) crystal planes of $Cu_{1.95}S$ (PDF# 89-2072), respectively. This indicated that the photocatalyst contained a certain amount of surface Cu vacancies. For the Cu_2S_{1-x} and Cu_2S, the XRD pattern showed characteristic features of cuprous sulfide (PDF# 02-1294), whose diffraction peaks at 37.82°, 46.51°, and 48.82° were ascribed to the (1 3 9), (5 7 3), and (4 11 2) crystal planes. Notably, the diffraction peak intensities of Cu_2S and Cu_2S_{1-x} were much stronger than those of $Cu_{1.95}S_{1-x}$. According to the previous report, this should be due to the existence of the inherent abundant vacancies on $Cu_{1.95}S$. Besides, the EPR spectroscopy also confirmed the surface S vacancies on Cu_2S, Cu_2S_{1-x}, and $Cu_{1.95}S_{1-x}$. Fig. 1b showed that $Cu_{1.95}S_{1-x}$ and Cu_2S_{1-x} both expressed obvious EPR signals at g = 2.002, which was associated with the S vacancies as the typical anion vacancy [16,17]. However, no EPR signal was observed over Cu_2S, suggesting the absence of S vacancy on Cu_2S. The experimental results in Fig. 1a and b indicated that the Cu and S dual vacancies existed on the surface of $Cu_{1.95}S_{1-x}$.

XPS was used to confirm the surface compositions and valence states of the as-prepared photocatalysts. For the Cu 2p spectrum in Fig. 2c, the characteristic peaks located at 933.27 ~ 934.26 eV (Cu $2p_{3/2}$) and 954.04 ~ 955.03 eV (Cu $2p_{1/2}$) were assigned to Cu^{2+}, and the distinct peaks at 932.12 ~ 932.23 eV (Cu $2p_{3/2}$) and 951.91 ~ 952.02 eV (Cu $2p_{1/2}$) were ascribed to Cu^{1+}. Notably, it could be observed that the binding energy of $Cu_{1.95}S_{1-x}$ shifted to the direction of low energy due to the existence of the surface Cu and S dual vacancies compared with Cu_2S and Cu_2S_{1-x}. And the slight shift of the peaks of Cu_2S_{1-x} compared to those of Cu_2S was also due to its surface S vacancies [13]. For the S 2p spectrum in Fig. 2d, compared with the two peaks at 161.59 and 162.99 eV related to S $2p_{3/2}$ and S $2p_{1/2}$ species of Cu_2S, new peaks appeared at 162.24 and 162.51 eV of Cu_2S_{1-x} and $Cu_{1.95}S_{1-x}$ respectively were because of the surface S vacancies. And the peaks at 168.39 eV of Cu_2S, Cu_2S_{1-x}, and $Cu_{1.95}S_{1-x}$ were assigned to the surface

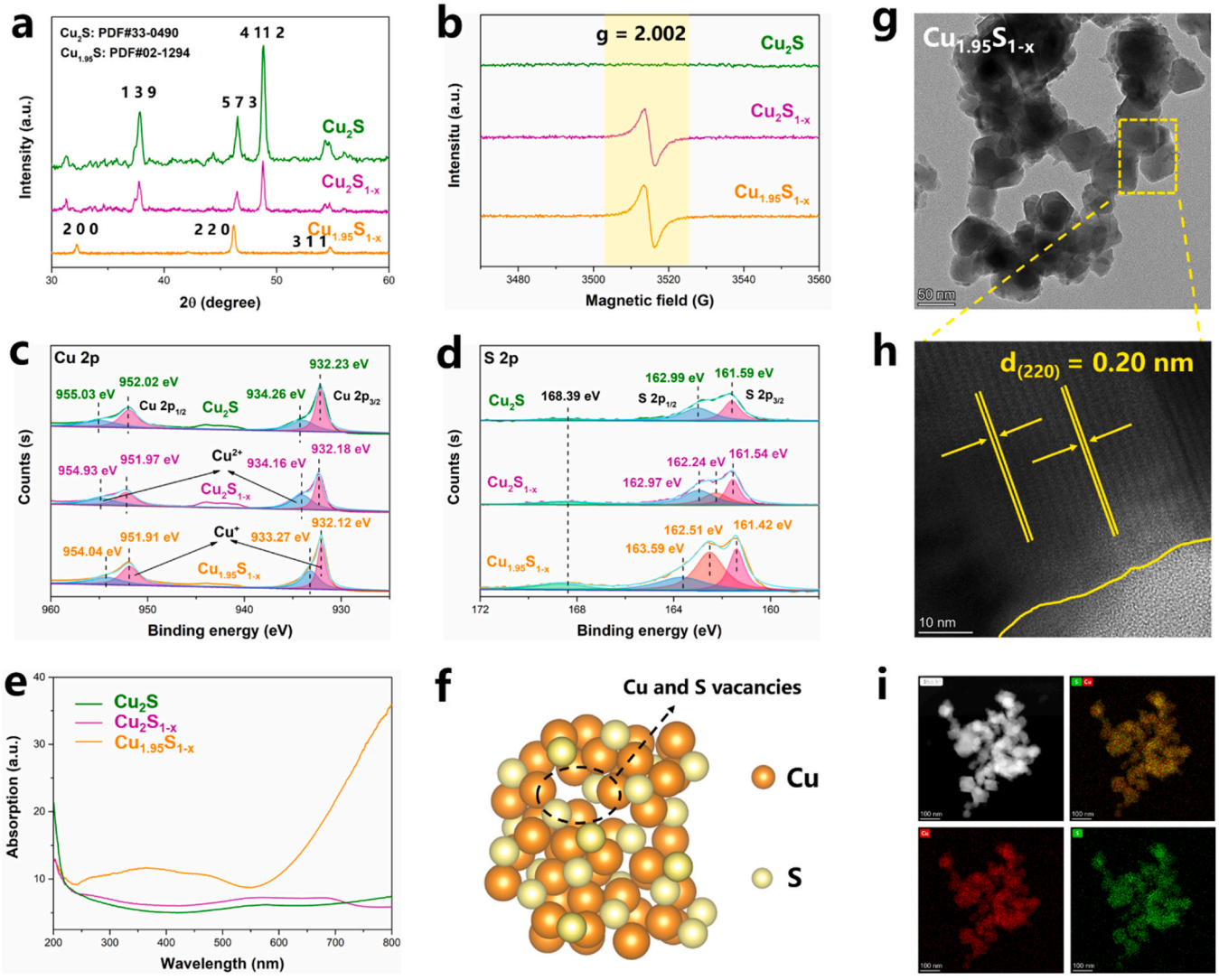

Fig. 1. XRD patterns of Cu_2S, Cu_2S_{1-x}, and $Cu_{1.95}S_{1-x}$ (a); EPR signals of S vacancies (b); XPS patterns of Cu_2S, Cu_2S_{1-x}, and $Cu_{1.95}S_{1-x}$: Cu 2p (c) and S 2p (d); UV–vis DRS of Cu_2S, Cu_2S_{1-x}, and $Cu_{1.95}S_{1-x}$ (e); Structural model of Cu_2S with Cu and S vacancies (f); HRTEM patterns of $Cu_{1.95}S_{1-x}$ (g, h); EDS mapping of $Cu_{1.95}S_{1-x}$, HAADF (white), Cu and S elements (yellow), Cu element (red) and S element (green) (i).

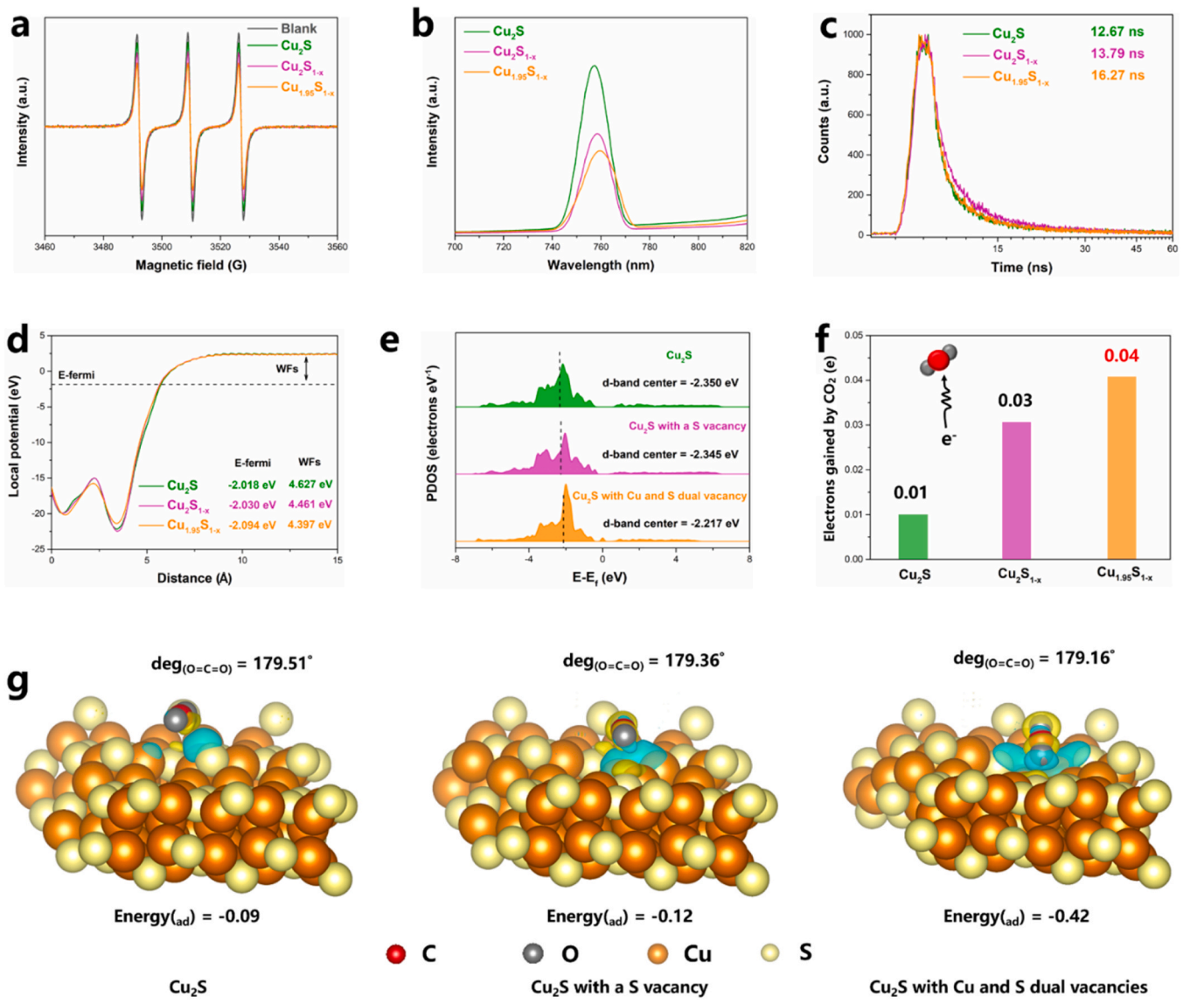

Fig. 2. EPR signals of electrons (a); PL spectra (b); Time-resolved transient PL decay, the values of abscissa (time) are logarithmically treated (c) of Cu_2S, Cu_2S_{1-x}, and $Cu_{1.95}S_{1-x}$; WFs (d); PDOS and D-band centers (e); Electrons gained by adsorbed CO_2 simulated by Bader analysis (f); The charge density difference of Cu_2S, Cu_2S with S vacancy, and Cu_2S with Cu and S dual vacancies, energy $_{(ad)}$ represented the adsorption energy, the isosurfaces were set to 0.003 e $Å^{-1}$ (g).

sulfate species (SO_x) [18]. The UV–vis DRS showed that the Cu_2S exhibited a weak full-spectrum absorption(Fig. 2e). While for Cu_2S_{1-x}, its absorption intensity was stronger than that of Cu_2S due to the surface S vacancies. However, after introducing the surface Cu and S dual vacancies, $Cu_{1.95}S_{1-x}$ enabled an enhanced optical absorption property as expected. As such, more photoinduced charge carriers would be available to be utilized [19]. On the basis of the above results, the structure models of pristine Cu_2S, Cu_2S with S vacancy (the structural model of Cu_2S_{1-x}), and Cu_2S with Cu vacancy and S vacancy (the structural model of $Cu_{1.95}S_{1-x}$) simulated by DFT calculation were shown in Figs. S1, S2, and 1f, respectively.

In addition, HRTEM was used to confirm the morphology and inner microstructure of these as-prepared cuprous sulfide photocatalysts. The $Cu_{1.95}S_{1-x}$ exhibited the structure of small ultrathin flakes in Fig. 1g, while the Cu_2S_{1-x} and Cu_2S were the large flaky structures (Figs. S3 and S4). We supposed that the CO_2 adsorption and charge transfer might benefit from the ultrathin structure of defective state $Cu_{1.95}S_{1-x}$. Fig. 1f shows the lattice fringes with an interplanar spacing of 0.20 nm, which was attributed to the (106) plane of $Cu_{1.95}S_{1-x}$. As for Cu_2S_{1-x} and Cu_2S, the HRTEM showed the interplanar spacing of 0.22 nm (Figs. S5 and S6), which were assigned to their (220) crystal planes [13,20]. The energy dispersive spectroscopy (EDS) mapping of $Cu_{1.95}S_{1-x}$ in Fig. 1f showed that the Cu and S elements were distributed uniformly across the whole $Cu_{1.95}S_{1-x}$ photocatalyst, which was in agreement with the XPS measurement results.

3.2. *The effect of Cu and S dual vacancies on photogenerated charge carrier transformation*

To study how the Cu and S dual vacancies on $Cu_{1.95}S_{1-x}$ affected its charge carrier transformation, we first measured the generation abilities of the photogenerated electrons. As shown in Fig. 2a, the Cu and S dual vacancies with abundant localized electrons on the surface of $Cu_{1.95}S_{1-x}$ resulted in the lowest EPR signals, corresponding to a higher electron consumption compared with Cu_2S_{1-x} and Cu_2S [21,22]. The transient photocurrent responses in Fig. S7 showed that the photocurrent signals generated by $Cu_{1.95}S_{1-x}$ were significantly higher than those of Cu_2S_{1-x} and Cu_2S, suggesting the inherent higher separation efficiency of electron-hole pairs of $Cu_{1.95}S_{1-x}$. The arc radius of $Cu_{1.95}S_{1-x}$ further confirmed this with an obviously reduced diameter in the Nyquist plot of

EIS (Fig. S8) [23–27]. The room temperature steady-state PL spectroscopy was used to explore the charge carrier kinetics of the as-prepared samples (Fig. 2b). Vacancy-free Cu_2S possessed the most intense peak in the steady-state PL, while the PL emission peak of $Cu_{1.95}S_{1-x}$ was obviously weaker than those of Cu_2S_{1-x} and Cu_2S. Thus, Cu and S dual vacancies of $Cu_{1.95}S_{1-x}$ were more dependable in inhibiting the recombination of photogenerated electron-hole pairs than the S vacancies of Cu_2S_{1-x} and vacancy-free Cu_2S. The time-resolved PL spectroscopy in Fig. 2c demonstrated that Cu_2S possessed a single lifetime component, suggesting the direct recombination of photogenerated electron-hole pairs with a lifetime $\tau(Cu_2S)$ of 12.67 ns. With the introduction of S vacancies, the lifetime ($\tau(Cu_2S_{1-x})$) of charge carriers was extended to 13.79 ns for Cu_2S_{1-x} for the S vacancies transiently trapped in the photogenerated electrons. Impressively, $Cu_{1.95}S_{1-x}$ displayed the longest lifetime ($\tau Cu_{1.95}S_{1-x}$) of 16.27 ns, indicating that Cu and S dual vacancies could provide more reliable photoelectron-trapping centers to inhibit the recombination of charge carriers [28,29].

DFT calculations were performed to study the charge carrier behavior at theoretical level. From the electronic work functions (Fig. 2d), one could see that Cu_2S with Cu and S dual vacancies with the minimum WF value (4.397 eV) compared with vacancy-free Cu_2S (4.627 eV) and Cu_2S with S vacancy (4.461 eV) indicated a lower barrier for photogenerated electron transfer, which was in agreement with the improved electronic transmission ability of $Cu_{1.95}S_{1-x}$ [30]. We have further investigated the partial density of states (PDOS) corresponding D-band center of surface Cu atoms as adsorption sites of these three models, as shown in (Fig. 2e). Compared with vacancy-free Cu_2S, introducing S vacancy on Cu_2S downshifted the Cu D-band center from − 2.350 eV to − 2.345 eV. Notably, the Cu and S dual vacancies on Cu_2S further downshifted the D-band center to − 2.217 eV, enabling the D-band center of Cu_2S with Cu and S dual vacancies to close to the Fermi energy level and leading to a better adsorption activity [13]. Furthermore, on the three photocatalysts, one could see that the CO_2 adsorbed on Cu_2S with Cu and S dual vacancies gained more electrons (0.04 e) than those adsorbed on vacancy-free Cu_2S (0.01 e) and Cu_2S with S vacancy (0.03 e), suggesting a desirable initial CO_2 activation of $Cu_{1.95}S_{1-x}$ (Fig. 2f). It is known that the activation of CO_2 could be reflected by the change of the angles of C═O double bond. It was found that after adsorbing, the C═O bond angle of CO_2 decreased from 179.51° (vacancy-free Cu_2S) and 179.36° (Cu_2S with S vacancy) to 179.16° (Cu_2S with Cu and S dual vacancies), disclosing the efficient activation of CO_2 on $Cu_{1.95}S_{1-x}$ [31]. The CO_2 adsorption on Cu_2S with Cu and S dual vacancies was indeed favored by the most negative adsorption free energy (−0.42 eV), in comparison to − 0.12 eV for Cu_2S with S vacancy and − 0.09 eV for vacancy-free Cu_2S, respectively, indicating an enhanced CO_2 adsorption ability, which was in agreement with the results of the D-band center calculation. The charge density difference was calculated to understand the charge distribution after CO_2 adsorption. There existed an obvious charge transfer between CO_2 and Cu_2S with Cu and S dual vacancies compared with vacancy-free Cu_2S and Cu_2S with S vacancy (Fig. 2g). Taken together, the above results suggested that the Cu and S deficient $Cu_{1.95}S_{1-x}$ represented the optimal photocatalyst for

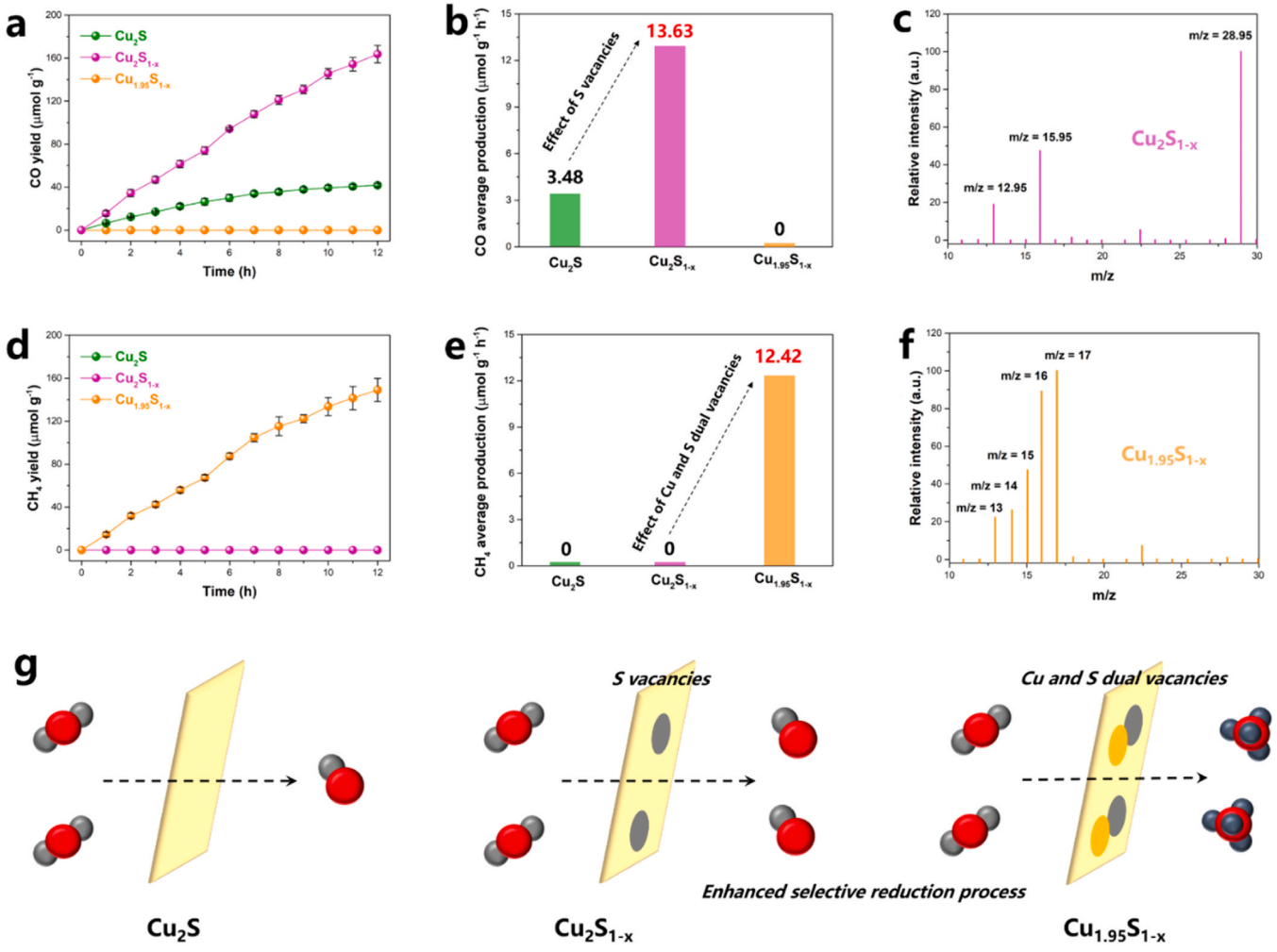

Fig. 3. CO (a, b) and CH_4 (d, e) yield of Cu_2S, Cu_2S_{1-x}, and $Cu_{1.95}S_{1-x}$; $^{13}CO_2$ isotopic labeling experiments for Cu_2S_{1-x} and $Cu_{1.95}S_{1-x}$ (c, f); Enhanced selective CO_2 photoreduction process promoted by Cu vacancies or Cu and S dual vacancies (g).

CO_2 adsorption and activation, which might contribute to photocatalytic CO_2 conversion.

3.3. Product selectivity regulated by Cu and S dual vacancies during CO_2 photoreduction reaction

With all of the above advantages, we believe the surface vacancies on Cu_2S could enable it to be an advanced catalyst for CO_2 photoreduction. As expected, in Figs. 3a and S9, the CO_2 photoreduction tests over Cu_2S and Cu_2S_{1-x} revealed that the sole product was CO. And with the introduction of the surface S vacancies, the CO produced by Cu_2S_{1-x} (163.56 μmol g^{-1}) increased with the 12 h prolonging illumination time, and much higher CO production than that of Cu_2S (41.76 μmol g^{-1}) was achieved, suggesting that S vacancies could promote the photocatalytic conversion of CO_2-to-CO (Fig. 3b). However, noteworthily, it was observed that CH_4 (149.04 μmol g^{-1}) was exclusively detected instead of CO over $Cu_{1.95}S_{1-x}$ (Figs. 3d and S9). This exciting phenomenon confirmed that the Cu and S dual vacancies could not only enhance the CO_2 photoreduction capacity, but efficiently switch the product selectivity from CO to CH_4 (Fig. 3e). This conclusion was further verified by the $^{13}CO_2$ isotopic labeling experimental results (Fig. 3c and f, Tables S1 and S2). The CO_2 photoreduction ability and product selectivity of $Cu_{1.95}S_{1-x}$ was compared with some photocatalysts (Table S3). In addition, the as-prepared photocatalysts showed no hydrocarbon products with pure Ar under 12 h illumination, indicating that CO_2 was the only carbon source during the CO_2 photoreduction process. No CO or CH_4 was detected without the photocatalysts, demonstrating that the photocatalyst played an essential role in CO_2 photoreduction (Figs. S10 and S11). The TEM pattern of the $Cu_{1.95}S_{1-x}$ after photocatalysis confirmed its good stability (Fig. S12). The results shown in this part fully proved that the surface S vacancies on Cu_2S_{1-x} could enhance the selective photoreduction of CO_2-to-CO, while the Cu and S dual vacancies on $Cu_{1.95}S_{1-x}$ enable the product selectivity switching from CO-to-CH_4, promoting the selective CO_2 photoreduction to produce products with higher added value (Fig. 3f).

3.4. Photocatalytic mechanism exploration of selective CO_2 reduction promoted by Cu and S dual vacancies

The in-situ FTIR was employed to explore and analyze the photocatalytic mechanism. The first step (0–30 min) was to ensure the CO_2/H2O mixture adsorption reached saturation in the dark, whereas the second step (10–50 min) was to detect the intermediate products of CO_2 photoreduction over the catalysts under light illumination. As shown in Fig. 4a and b, the in-situ FTIR of Cu_2S and Cu_2S_{1-x} revealed multiple intermediate products, including activated CO_2 (CO_2^-, 1245 and 1690 cm^{-1}), b-CO_3^{2-} (1346 cm^{-1}) and HCO_3^- (1443 and 1478 cm^{-1}). COOH* (1212 and 1610 cm^{-1}) was monitored as an important intermediate for CO production, suggesting the CO_2 → COOH* → CO photoreduction process [32–35]. The new CO_2^- peak appeared at 1245 cm^{-1} was due to the enhanced CO_2 activation promoted by S vacancies. Different intermediates demonstrated a different photocatalytic CO_2 reduction system for $Cu_{1.95}S_{1-x}$ (Fig. 4c). The CO_2^- (1239 and 1692 cm^{-1}), b-CO_3^{2-} (1365 cm^{-1}), and HCO_3^- (1441 and 1487 cm^{-1}) were observed. COOH* (1210 and 1608 cm^{-1}) was detected as the intermediate product for HCOOH* (1553 cm^{-1}) production. The HCOOH*

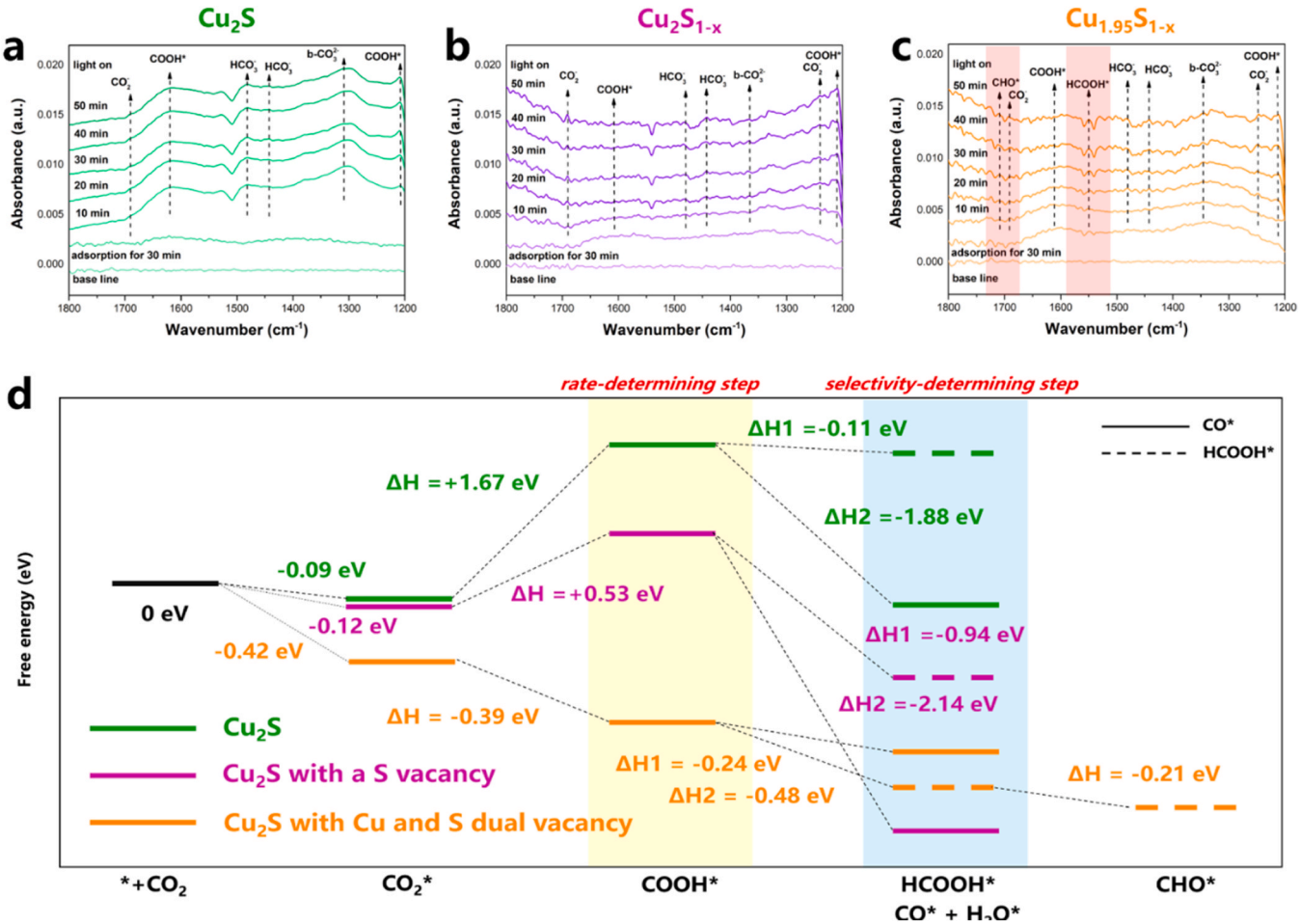

Fig. 4. In-situ FTIR of Cu_2S, Cu_2S_{1-x}, and $Cu_{1.95}S_{1-x}$ (a-c); Reaction pathways of CO_2 photoreduction over Cu_2S, Cu_2S with S vacancy, and Cu_2S with Cu and S dual vacancies based on DFT calculation. Asterisk (*) represented the adsorption site on the substrate (d).

was further reduced to CHO* (1710 cm^{-1}) as the key intermediate for CH_4 production, suggesting a different reduction pathway compared with Cu_2S and Cu_2S_{1-x} [36–40]. Based on the above experimental results, the reaction energies of the possible intermediates over samples were calculated. As shown in Fig. 4d, the CO_2 adsorbed on Cu_2S with Cu and S dual vacancies was indeed favored by the most negative adsorption free energy for the initial CO_2 activation (CO_2*), in comparison to Cu_2S and Cu_2S with S vacancy. The CO_2* → COOH* is generally regarded as the rate-determining step for CO* or HCOOH* production. This energy barrier varied among these samples that decreased from + 1.67 eV for Cu_2S to + 0.53 eV for Cu_2S with S vacancy, indicating that the single S vacancy could lower the energy barrier. However, − 0.39 eV of this step for Cu_2S with Cu and S vacancies suggested that under the effect of Cu and S dual vacancies, the reaction of the CO_2* → COOH* was transformed from endothermic to exothermic, indicating that the Cu and S dual vacancies could enable the spontaneous CO_2* → COOH* process. Two pathways (COOH* → CO* or COOH* → HCOOH*) existed in the next step, for Cu_2S and Cu_2S with S vacancy, the transition from COOH* → CO* was more favorable than COOH* → HCOOH*. While with the introduction of a Cu vacancy, the selectivity was efficiently switched from CO* to HCOOH*, and HCOOH* was further spontaneously reduced to CHO* as the key intermediate product for CH_4 generation. The calculated structures and values were demonstrated in Figs. S13 to S15 and Table S4. Combining the experimental and theoretical calculation results, we confirmed that the Cu and S dual vacancies on $Cu_{1.95}S_{1-x}$ could promote the CO_2 photoreduction process and efficiently adjust the product selectivity to gain pure CH_4 product.

4. Conclusions

In summary, to both improve the activity and modulate the product selectivity of CO_2 photoreduction, we designed three kinds of copper sulfide photocatalysts. With the surface S vacancies, Cu_2S_{1-x} exhibited a high performance for CO production compared with the vacancy-free Cu_2S. On the one hand, the Cu vacancies in $Cu_{1.95}S_{1-x}$ efficiently adjust the pathways during the CO_2 photoreduction process, and CH_4 was detected as the only product. These favorable features combined give rise to the preferential formation of CH_4 of higher value instead of CO. Moreover, the Cu and S vacancies also boosted the charge transfer, provided more surface active sites, enhanced the CO_2 adsorption capacity, and lowered the energy barriers of rate-determining and selectivity-determining steps, thus improving the CO_2 photoreduction activity of $Cu_{1.95}S_{1-x}$. We believe the strategy presented in this work can be used for other copper-based catalysts to produce different value-added carbon-based products with high performance and selectivity.

CRediT authorship contribution statement

Xian Shi and **Jianping Sheng:** Formal analysis, Methodology, Investigation,Writing – original draft. **Xing'an Dong** and **Weidong Dai:** Methodology, Validation, Investigation. **Qin Ren**: Investigation, Methodology. **Fan Dong:** Conceptualization, Supervision, Project administration, Funding acquisition.

Declaration of Competing Interest

The authors declare that they have no known competing financial interests or personal relationships that could have appeared to influence the work reported in this paper.

Data availability

Data will be made available on request.

Acknowledgements

This work was supported by National Natural Science Foundation of China (52200123, 22225606, and 22261142663), Excellent Youth Foundation of Sichuan Scientific Committee (2021JDJQ0006).

Appendix A. Supporting information

Supplementary data associated with this article can be found in the online version at doi:10.1016/j.apcatb.2023.123147.

References

[1] F. Chen, H. Huang, L. Ye, T. Zhang, Y. Zhang, Thickness-dependent facet junction control of layered $BiOIO_3$ single crystals for highly efficient CO_2 photoreduction, Adv. Funct. Mater. (28) (2018), 1804284.
[2] Y. Tamaki, T. Morimoto, K. Koike, O. Ishitani, Photocatalytic CO_2 reduction with high turnover frequency and selectivity of formic acid formation using Ru(II) multinuclear complexes, Proc. Natl. Acad. Sci. USA (109) (2012) 15673–15678.
[3] P. Wang, J. Wang, X. An, J. Shi, W. Shangguan, X. Hao, G. Xu, B. Tang, A. Abudula, G. Guan, Generation of abundant defects in Mn-Co mixed oxides by a facile agar-gel method for highly efficient catalysis of total toluene oxidation, Appl. Catal. B Environ. (282) (2021), 119560.
[4] D. Gao, I.T. McCrum, S. Deo, Y.W. Choi, F. Scholten, W. Wan, J.G. Chen, M. J. Janik, B. Roldan Cuenya, Activity and selectivity control in CO_2 electroreduction to multicarbon products over CuO_x catalysts via electrolyte design, ACS Catal. (8) (2018) 10012–10020.
[5] H. Li, J. Shang, Z. Ai, L. Zhang, Efficient visible light nitrogen fixation with BiOBr nanosheets of oxygen vacancies on the exposed {001} facets, J. Am. Chem. Soc. (137) (2015) 6393–6399.
[6] J. Liu, J. Ke, D. Li, H. Sun, P. Liang, X. Duan, W. Tian, M.O. Tadā, S. Liu, S. Wang, Oxygen vacancies in shape controlled Cu_2O/reduced graphene oxide/In_2O_3 hybrid for promoted photocatalytic water oxidation and degradation of environmental pollutants, ACS Appl. Mater. Interfaces (9) (2017) 11678–11688.
[7] C. Gao, Q. Meng, K. Zhao, H. Yin, D. Wang, J. Guo, S. Zhao, L. Chang, M. He, Q. Li, H. Zhao, X. Huang, Y. Gao, Z. Tang, Co_3O_4 Hexagonal platelets with controllable facets enabling highly efficient visible-light photocatalytic reduction of CO_2, Adv. Mater. (28) (2016) 6485–6490.
[8] J. Fu, K. Jiang, X. Qiu, J. Yu, M. Liu, Product selectivity of photocatalytic CO_2 reduction reactions, Mater. Today (32) (2020) 222–243.
[9] L. Wan, Q. Zhou, X. Wang, T.E. Wood, G.A. Ozin, Cu_2O nanocubes with mixed oxidation-state facets for (photo)catalytic hydrogenation of carbon dioxide, Nat. Catal. (2) (2019) 889–898.
[10] F. Zhao, Y. Feng, Y. Wang, X. Zhang, W. Feng, Two-dimensional gersiloxenes with tunable bandgap for photocatalytic H_2 evolution and CO_2 photoreduction to CO, Nat. Commun. (11) (2020) 1443.
[11] X. Jiao, Z. Chen, X. Li, Y. Sun, S. Gao, W. Yan, C. Wang, Q. Zhang, Y. Lin, Y. Luo, Y. Xie, Defect-mediated electron-hole separation in one-unit-cell $ZnIn_2S_4$ layers for boosted solar-driven CO_2 reduction, J. Am. Chem. Soc. (139) (2017) 7586–7594.
[12] Y. Zhang, B. Xia, J. Ran, K. Davey, S.Z. Qiao, Atomic-level reactive sites for semiconductor-based photocatalytic CO_2 reduction, Adv. Energy Mater. (10) (2020), 1903879.
[13] S. Li, H. Duan, J. Yu, C. Qiu, R. Yu, Y. Chen, Y. Fang, X. Cai, S. Yang, Cu vacancy induced product switching from formate to CO for CO_2 reduction on copper sulphide, ACS Catal. (12) (2022) 9074–9082.
[14] C. Peng, G. Luo, J. Zhang, M. Chen, Z. Wang, T. Sham, L. Zhang, Y. Li, G. Zheng, Double sulphur vacancies by lithium tuning enhance CO_2 electroreduction to n-propanol, Nat. Commun. (12) (2021) 1580.
[15] Z. Yang, Y. Shi, H. Li, C. Mao, X. Wang, X. Liu, X. Liu, L. Zhang, Oxygen and chlorine dual vacancies enable photocatalytic O_2 dissociation into monatomic reactive oxygen on BiOCl for refractory aromatic pollutant removal, Environ. Sci. Technol. 56 (2022) 3587–3595.
[16] Q. Ren, Y. He, H. Wang, Y. Sun, F. Dong, Photo-switchable oxygen vacancy as the dynamic active site in the photocatalytic NO oxidation reaction, ACS Catal. (12) (2022) 14015–14025.
[17] X. Dong, Z. Cui, Y. Sun, F. Dong, Humidity-independent photocatalytic toluene mineralization benefits from the utilization of edge hydroxyls in layered double hydroxides (LDHs): a combined operando and theoretical investigation, ACS Catal. (11) (2021) 8132–8139.
[18] Z. Zhang, J. Sun, S. Mo, J. Kim, D. Guo, J. Ju, Q. Yu, M. Liu, Constructing a highly efficient CuS/Cu_9S_5 heterojunction with boosted interfacial charge transfer for near-infrared photocatalytic disinfection, Chem. Eng. J. (431) (2022), 134287.
[19] S. Gao, B.C. Gu, X.C. Jiao, Y.F. Sun, X.L. Zu, F. Yang, W.G. Zhu, C.M. Wang, Z. M. Feng, B.J. Ye, Y. Xie, Highly efficient and exceptionally durable CO_2 photoreduction to methanol over freestanding defective single-unit-cell bismuth vanadate layers, J. Am. Chem. Soc. 139 (2017) 3438–3445.
[20] Y. Zhao, H. Pan, Y. Lou, X. Qiu, J. Zhu, C. Burda, Plasmonic $Cu_{2-x}S$ nanocrystals: optical and structural properties of copper-deficient copper (I) sulphides, J. Am. Chem. Soc. (131) (2009) 4253–4261.
[21] K. Bhattacharyya, G.P. Mane, V. Rane, A.K. Tripathi, A.K. Tyagi, Selective CO_2 photoreduction with Cu-doped TiO_2 photocatalyst: delineating the crucial role of

Cu-oxidation state and oxygen vacancies, J. Phys. Chem. C (125) (2021) 1793–1810.
[22] J. Di, Z. Chao, M. Ji, M. Duan, L. Ran, Y. Cheng, K. Guo, X. Jun, Y. She, J. Xia, H. Li, Z. Liu, Defect-rich $Bi_{12}O_{17}Cl_2$ nanotubes self-accelerating charge separation for boosting photocatalytic CO_2 reduction, Angew. Chem. Int. Ed. (57) (2018) 14847–14851.
[23] L. Ye, W. Hui, X. Jin, Y. Su, D. Wang, H. Xie, X. Liu, X. Liu, Synthesis of olive-green few-layered BiOI for efficient photoreduction of CO_2 into solar fuels under visible/near-infrared light, Sol. Energ. Mat. Sol. C (144) (2016) 732–739.
[24] P. Chen, H. Liu, Y. Sun, J. Li, F. Dong, Bi metal prevents the deactivation of oxygen vacancies in $Bi_2O_2CO_3$ for stable and efficient photocatalytic NO abatement, Appl. Catal. B Environ. (264) (2019), 118545.
[25] S. Cao, B. Shen, T. Tong, J. Fu, J. Yu, 2D/2D heterojunction of ultrathin MXene/Bi_2WO_6 nanosheets for improved photocatalytic CO_2 reduction, Adv. Funct. Mater. (28) (2018) 1800136.
[26] M. Guan, C. Xiao, Z. Jie, S. Fan, R. An, Q. Cheng, J. Xie, Z. Min, B. Ye, Y. Xie, Vacancy associates promoting solar-driven photocatalytic activity of ultrathin bismuth oxychloride nanosheets, J. Am. Chem. Soc. (135) (2013) 10411–10417.
[27] B. Su, M. Zheng, W. Lin, X. Lu, D. Luan, S. Wang, X. Lou, S-scheme Co_9S_8@$Cd_{0.8}Zn_{0.2}S$-DETA hierarchical nanocages bearing organic CO_2 activators for photocatalytic syngas production, Adv. Energy Mater. (13) (2023), 2203290.
[28] G. Chen, F. Wei, Z. Zhou, B. Su, C. Yang, X. Lu, S. Wang, X. Wang, Phase junction crystalline carbon nitride nanosheets modified with CdS nanoparticles for photocatalytic CO_2 reduction, Sustain. Energy Fuels (7) (2023) 381–388.
[29] F. Wei, W. Xue, Z. Yu, X. Lu, S. Wang, W. Lin, X. Wang, Dynamic cooperations between lattice oxygen and oxygen vacancies for photocatalytic ethane dehydrogenation by a self-restoring $LaVO_4$ catalyst, Chin. Chem. Lett. (2023), 108313.
[30] X. Wang, C. Zhou, L. Yin, R. Zhang, G. Liu, Iodine-deficient BiOI nanosheets with lowered valence band maximum to enable visible light photocatalytic activity, ACS Sustain. Chem. Eng. (7) (2019) 7900–7907.
[31] X. Jin, C. Lv, X. Zhou, H. Xie, S. Sun, Y. Liu, Q. Meng, G. Chen, A bismuth rich hollow $Bi_4O_5Br_2$ photocatalyst enables dramatic CO_2 reduction activity, Nano Energy (64) (2019), 103955.
[32] J. Sheng, Y. He, J. Li, C. Yuan, F. Dong, F, Identification of halogen-associated active sites on bismuth-based perovskite quantum dots for efficient and selective CO_2-to-CO photoreduction, ACS Nano (14) (2020) 13103–13114.
[33] Y. Li, B. Li, D. Zhang, L. Cheng, Q. Xiang, Crystalline carbon nitride supported copper single atoms for photocatalytic CO_2 reduction with nearly 100% CO selectivity, ACS Nano (14) (2020) 10552–10561.
[34] G. Gao, Y. Jiao, E.R..Waclawik, A. Du, Single atom (Pd/Pt) supported on graphitic carbon nitride as an efficient photocatalyst for visible-light reduction of carbon dioxide, J. Am. Chem. Soc., (138) 20166 292–6297.
[35] Y. Wang, J. Zhao, T. Wang, Y. Li, X. Li, J. Yin, C. Wang, CO_2 photoreduction with H_2O vapor on highly dispersed CeO_2/TiO_2 catalysts: surface species and their reactivity, J. Catal. (337) (2016) 293–302.
[36] D. Ren, R. Shen, Z. Jiang, X. Lu, X. Li, Highly efficient visible-light photocatalytic H_2 evolution over ^{2}D–^{2}D CdS/Cu_7S_4 layered heterojunctions, Chin. J. Catal. (41) (2020) 31–40.
[37] L. Cheng, D. Zhang, Y. Liao, J. Fan, Q.J. Xiang, Structural engineering of 3D hierarchical $Cd_{0.8}Zn_{0.2}S$ for selective photocatalytic CO_2 reduction, Chin. J. Catal. (42) (2021) 31–140.
[38] Y. Li, B. Li, D. Zhang, L. Cheng, Q. Xiang, Crystalline carbon nitride supported copper single atoms for photocatalytic CO_2 reduction with nearly 100% CO selectivity, ACS Nano (14) (2020) 10552–10561.
[39] M. Wang, M. Shen, X. Jin, J. Tian, M. Li, Y. Zhou, L. Zhang, Y. Li, J. Shi, Oxygen vacancy generation and stabilization in CeO_{2-x} by Cu-introduction with improved CO_2 photocatalytic reduction activity, ACS Catal. (9) (2019) 4573–4581.
[40] R. Long, Y. Li, Y. Liu, S. Chen, X. Zheng, C. Gao, C. He, N. Chen, Z. Qi, L. Song, J. Jiang, J. Zhu, Y. Xiong, Isolation of Cu atoms in Pd lattice: forming highly selective sites for photocatalytic conversion of CO_2 to CH_4, J. Am. Chem. Soc. (139) (2017) 4486–4492.